

Construction of iron-mineralized black phosphorene nanosheet to combine chemodynamic therapy and photothermal therapy

Zhaoqing Shi^a, Jing Tang^a, Chuchu Lin^a, Ting Chen^a, Fan Zhang^b, Yuxing Huang^c, Ping Luan^d, Zhuo Xin^c, Qianqian Li^e and Lin Mei^{a,b}

^aSchool of Pharmaceutical Sciences (Shenzhen), Sun Yat-sen University, Shenzhen, China; ^bTianjin Key Laboratory of Biomedical Materials, Key Laboratory of Biomaterials and Nanotechnology for Cancer Immunotherapy, Institute of Biomedical Engineering, Chinese Academy of Medical Sciences and Peking Union Medical College, Tianjin, China; ^cSchool of Material Science and Engineering and Institute for Advanced Study, Nanchang University, Nanchang, China; ^dGuangdong Second Provincial General Hospital and Health Science Center, Shenzhen University, Shenzhen, China; ^eShenzhen Bay Laboratory, Shenzhen, China

ABSTRACT

Chemodynamic therapy (CDT) by triggering Fenton reaction or Fenton-like reaction to generate hazardous hydroxyl radical ($\bullet\text{OH}$), is a promising strategy to selectively inhibit tumors with higher H_2O_2 levels and relatively acidic microenvironment. Current Fe-based Fenton nanocatalysts mostly depend on slowly releasing iron ions from Fe or Fe oxide-based nanoparticles, which leads to a limited rate of Fenton reaction. Herein, we employed black phosphorene nanosheets (BPNS), a biocompatible and biodegradable photothermal material, to develop iron-mineralized black phosphorene nanosheet (BPFe) by *in situ* deposition method for chemodynamic and photothermal combination cancer therapy. This study demonstrated that the BPFe could selectively increase cytotoxic $\bullet\text{OH}$ in tumor cells whereas having no influence on normal cells. The IC_{50} of BPFe for tested tumor cells was about 3–6 $\mu\text{g}/\text{mL}$, which was at least one order of magnitude lower than previous Fe-based Fenton nanocatalysts. The low H_2O_2 level in normal mammalian cells guaranteed the rare cytotoxicity of BPFe. Moreover, the combination of photothermal therapy (PTT) with CDT based on BPFe was proved to kill tumors more potently with spatiotemporal accuracy, which exhibited excellent anti-tumor effects in xenografted MCF-7 tumor mice models.

ARTICLE HISTORY

Received 10 January 2022
Revised 31 January 2022
Accepted 1 February 2022





KEYWORDS


Black phosphorene;
chemodynamic therapy;
drug delivery systems;
Fenton reaction;
photothermal therapy

1. Introduction

Over-production of H_2O_2 is a typical character of tumors, especially for solid malignance, which provides a promising biomarker to design selective anti-tumor therapeutics (Hanahan & Weinberg, 2011; Saravanakumar et al., 2017; Shi et al., 2020; Tang et al., 2021). In Fenton or Fenton-like reactions, H_2O_2 is catalyzed to hydroxyl radical ($\bullet\text{OH}$), which is the most hazardous oxidative radical with the oxidative potential of 2.73V (Trachootham et al., 2009; Liu et al., 2019). Chemodynamic therapy (CDT) based Fenton or Fenton-like reactions have the potential to selectively kill tumors with high-level H_2O_2 without the need of O_2 , which has advantages in treating solid tumors with hypoxic microenvironment (Trachootham et al., 2009; Lin et al., 2018). Recently, transition metals like iron (Zhang et al., 2016; Chen et al., 2020; Pan et al., 2020a), copper (Li et al., 2019; Wu et al., 2019) and manganese (Lin et al., 2018; Ding et al., 2020) have shown talent in inducing Fenton reactions to realize CDT.

Iron-based agents are the most widely employed materials as CDT agents among various transition metals because iron ions presented the highest Fenton catalytic efficiency (Zhang et al., 2016; Li et al., 2019; Chen et al., 2020). Currently, iron nano precipitates, iron oxide nanoparticles and iron mineral nanoparticles are developed to Fe-based CDT nano-systems (Huo et al., 2017; Liu et al., 2018; Chen et al., 2019; Fan et al., 2019; Lei et al., 2019; Pan et al., 2020a). These systems could degrade and release Fe ions in a tumor acidic environment. However, the amount of generated Fe ion species and the concentration of intracellular H_2O_2 are too low to induce a strong Fenton reaction (Dong et al., 2019; Wang et al., 2019). To solve these problems, Shi *et al.* designed NIR responsive iron oxide nanoparticles for enhancing the release of Fe ions, which achieved higher catalytic efficiency (Hu et al., 2017; Feng et al., 2019). Yeh *et al.* developed an H_2O_2 -loaded $\text{Fe}_3\text{O}_4@PLGA$ nano-system for enhancing CDT efficacy (Li et al., 2016) because the H_2O_2 could accelerate the release of Fe ions from iron oxides while providing substrates of Fenton reaction. These strategies improved the Fenton reaction efficacy by applying exogenous stimulation or increasing

CONTACT Lin Mei  meilin@bme.pumc.edu.cn  School of Pharmaceutical Sciences (Shenzhen), Sun Yat-sen University, Shenzhen, 518107, China; Qianqian Li  liqq_1993@163.com  Shenzhen Bay Laboratory, Shenzhen, 518055, China

 Supplemental data for this article can be accessed [here](#).

© 2022 The Author(s). Published by Informa UK Limited, trading as Taylor & Francis Group.

This is an Open Access article distributed under the terms of the Creative Commons Attribution License (<http://creativecommons.org/licenses/by/4.0/>), which permits unrestricted use, distribution, and reproduction in any medium, provided the original work is properly cited.

intracellular H_2O_2 concentration (Wang et al., 2020, 2021). More recently, Bu *et al.* synthesized amorphous Fe-based CDT agents for increasing the release rate of Fe ions, which showed enhanced Fenton reaction efficacy without exogenous stimulation (Chen et al., 2020). Therefore, it is evident that the Fe ions released from Fe-based nano-systems significantly determine the Fenton reaction efficacy (Hu et al., 2017). Compared with traditional iron oxide nanoparticles and iron mineral nanoparticles, novel nano-systems that are able to efficiently deliver and release Fe ions specifically at tumor sites should be developed.

Black phosphorene (BP), a kind of two-dimensional material, is a popular drug carrier for precise drug delivery because of its excellent photothermal ability, drug loading capacity and considerable biodegradability (Sun et al., 2015; Luo et al., 2019; Hu et al., 2020; Shi et al., 2020). BP is negatively charged, and it owns a high specific surface area, which can load drugs *via* electrostatic attraction and $\pi - \pi$ stack (Wang et al., 2015; Liu et al., 2019; Luo et al., 2019; 2019; Shi et al., 2020). Therefore, decorating positive charged cargos or drugs with aromatic structures on the surface of BP is widely applied (Tao et al., 2017; Zeng et al., 2018; Pan et al., 2020b; An et al., 2021). Recently, Yu *et al.* demonstrated an *in situ* mineralization for loading Ca^{2+} on BPNS, and such method gained enhanced ion loading capacity than the previous electrostatic attraction method. Moreover, BP is a biodegradable photothermal agent, which could be used for efficient photothermal therapy (PTT) and photothermal on-demand drug release (Kuntz et al., 2017; Tao et al., 2017; Qiu et al., 2018; Zeng et al., 2018; Li et al., 2019; Liang et al., 2019; Luo et al., 2020).

Considering the favorable characteristics of BP for loading cations, we rationally designed a kind of iron-mineralized black phosphorene nanosheets (BPFe) to deliver and on-demand release Fe ions to tumor sites, which achieved CDT and PTT combination cancer therapy (Figure 1). Compared with previous iron oxide-based nano-systems, the BPFe showed better Fenton catalytic efficacy because the loaded Fe ion species could be rapidly released at a tumor acidic environment. Owing to this unique property, our BPFe showed an excellent anti-tumor effect in MCF-7 xenograft mice models only relying on the overproduced H_2O_2 of tumor cells. Besides, BPFe exhibited good safety on normal cells and major organs with a lower level of H_2O_2 than that of tumor cells. Moreover, the BPFe preserved the excellent photothermal properties of BPNS, which could combine CDT and PTT with spatiotemporal accuracy.

2. Experimental section

2.1. Materials

Bulk black phosphorus crystal (purity > 99.9%) was purchased from Nanjing Muke Nanotechnology (Nanjing, China). Iron (II) chloride and aqueous ammonia were purchased from Shanghai Macklin Biochemical Co., Ltd (Shanghai, China). Doxorubicin hydrochloride, methylene blue and N-methylpyrrolidone (NMP) were purchased from Aladdin (Shanghai, China). DMEM-H, RPMI-1640, fetal bovine serum

(FBS), phosphate buffer saline of pH 7.2–7.4 (PBS), trypsin-EDTA, the penicillin-streptomycin solution were purchased from Gibco, Thermo Fisher Scientific. Cell counting kit-8 (CCK-8) was purchased from APEXBio Technology (Shanghai, China). H_2O_2 assay kit (S0038) and ROS assay kit (S0033) were purchased from Beyotime Biotechnology (Shanghai, China). $Fe_3O_4@PEI$ nanoparticle was obtained from Xi'an Ruixi Biological Technology (Xi'an, China). Annexin V-FITC/PI apoptosis detection kit and Calcein-AM live-cell staining kit were purchased from Solarbio Life Sciences (Beijing, China).

2.2. Preparation of BPNS, BPFe and BPFep

Our BPFep was prepared by means of top to bottom strategy (shown in Figure 1). The protocol required 3 steps: exfoliation of bulk BP, phosphorylation of BPNS and *in situ* mineralization of Fe ions. The exfoliation of BP was to obtain size uniformed BPNS, and the detailed method was referred to in our previous research (Zeng et al., 2018). The size uniformed BPNS was then monodispersed in NMP and the mixture was added with $NH_3 \cdot H_2O$ for phosphorylation, which was to transform the elemental phosphorus to negatively charged phosphate groups on BPNS surface (Pan et al., 2020b). Due to the strong association of phosphate with Fe ions, the Fe ions were simultaneously mineralized on the phosphate groups by gently adding $FeCl_2$ to produce BPFe.

BPNS was prepared by the sonication exfoliation method (Zeng et al., 2018). 100 mg powder of ground bulk BP crystal was dispersed in 80 mL of NMP and sonicated with a $\Phi = 6$ mm probe for 12 h in an ice bath under 650 W. Thereafter, the solution was then sonicated for 8 h under 600 W. Finally, BPNS with uniformed size was obtained by gradient centrifugation. The solution was centrifuged at 7000 rpm for 15 min to isolate large bulks, and the supernatant was collected for further centrifugation at 14,000 rpm for 20 min to obtain the BPNS precipitates.

BPFe was prepared by *in situ* mineralization method, which was detailedly shown in Figure 1a (Pan et al., 2020b). 5 mg of BPNS was dispersed in 100 mL of NMP (50 μ g/mL) and sonicated in the water bath to form a uniform dispersion, and then 100 μ L 28% aqueous ammonia was added to the solution to phosphorylate the surface of BPNS. The mixture was vigorously stirred at 37 $^{\circ}C$ for 2 h. To deposit the iron ions on the surface of BPNS, 5 mL $FeCl_2$ /ethanol solution with a feeding ratio of 1:20 was gently added into the mixture under the protection of argon for 12 h. Finally, the BPFe was collected by centrifugation and washed with ethanol several times. The as-prepared BPFe was vacuum dried or stored in ethanol for further use.

BPFep was prepared by the PEGylation method according to our previous research (Tao et al., 2017). In brief, 2 mg BPFe was dispersed in 1 mg/mL PEG- NH_2 aqueous solution, and the mixture was sonicated for 0.5 h *via* probe sonication. Then the mixture was stirred for another 3 h and the BPFep was obtained by centrifugation.

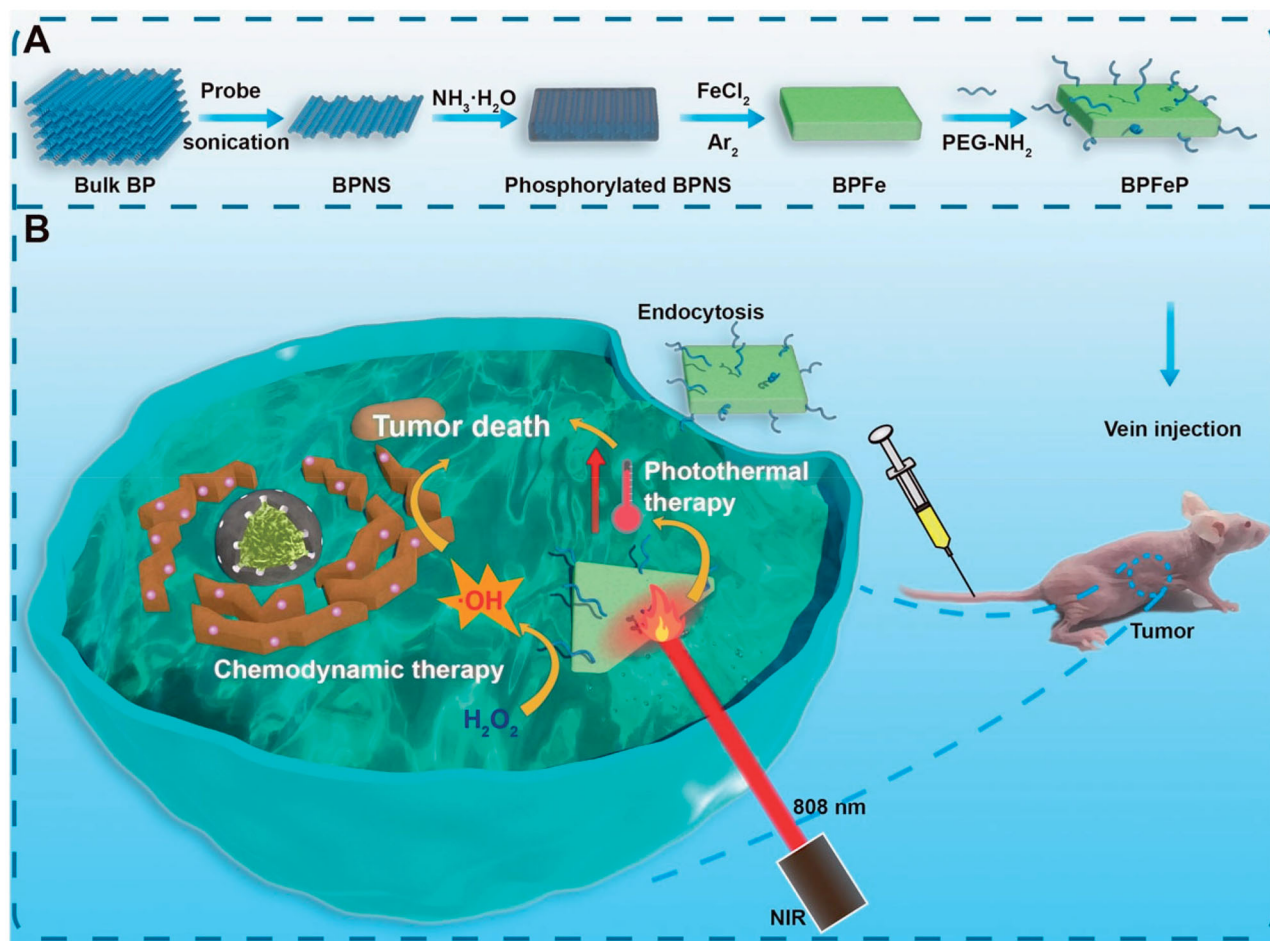


Figure 1. Schematic illustration of iron-mineralized black phosphorene (BPFe) for efficiently generating intracellular Fenton-reaction as an anti-tumor platform. (a) Preparation of BPFe: the bulk BP was exfoliated by probe sonication to obtain BPNS, and the FeCl_2 was mineralized on ammonia-phosphorylated BPNS to prepare BPFe, which was finally PEGylated to give BPFEP. (b) Mechanism of BPFEP for chemodynamic and photothermal combination therapy.

2.3. Characterization

Transmission electron microscope (TEM) images of BPNS and BPFe were performed on JEM-1400 to observe the morphology. EDS mapping was performed on JEM-F200 to observe the elemental distribution. Atom force microscopy (AFM) was employed to determine the thickness of nanosheets, which was measured by Nanoscope IIIa. Dynamic light scattering (DLS) and phase analysis scattering (PALS) were analyzed on Brookhaven NanoBrook 90Plus PALS to determine the hydrodynamic size and zeta potential of BPNS, BPFe and BPFEP.

XPS survey was tested by ESCALAB 250Xi to analyze the surface composition of BPFe. ICP-MS was employed for quantification of BPFe, and the UV-vis spectrophotometry was determined by PerkinElmer LAMBDA 365 to analyze optical properties and study the linear relationship between concentration and absorption. The photothermal property was conducted by an 808 nm diode laser fiber coupling system and Fluke Ti450 thermal imaging camera.

2.4. Cell culture

Tumor and normal cell lines were used in this study: MCF-7, human breast cancer cells; Hep1-6, murine hepatoma cells; B16-F10, murine melanoma cells; NCM460, normal human

colon mucosal epithelial cells. All the cells were purchased from CTCC and cultured by 89% DMEM-H (or RPMI-1640) + 10% FBS + 1% P/S in a 5% CO_2 balanced incubator at 37 °C.

2.5. Preparation of DOX-labeled BPFe and cellular uptake evaluation

To evaluate the cellular uptake of BPFe, we employed DOX as a fluorescent label for flow cytometry (FCM, Beckman Coulter CytoFLEX) and confocal laser scanning microscopy (ZEISS LSN880). To label DOX on the BPFe, 1 mg BPNS were dispersed in 20 mL NMP, and 0.1% aqueous ammonia was added. After 2 h, the DOX with a feeding ratio of 1:3 was carefully added into the mixture and stirred for 12 h to obtain BPFe@DOX. The BPFe@DOX was collected by centrifugation and washed several times.

The FCM was used to quantitatively determine the cellular uptake behavior, 10^5 cells were incubated in a 6-wells plate and treated with 20 $\mu\text{g}/\text{mL}$ BPFe@DOX at different time points. Finally, the cells were collected for FCM detection on the PC5.5 channel. The data was processed by CytExpert. The confocal laser scanning microscope (CLSM) was used to qualitatively observe the uptake of BPFe. The cells were seeded in the glass-bottom dish, and the incubated cells were observed by CLSM with a 488 nm laser.

2.6. Intracellular H₂O₂ concentration determination

The intracellular H₂O₂ concentration of tumor and normal cell lines was determined by the H₂O₂ assay kit. Briefly, the tumor and normal cell lines were cultured on a large scale and 10⁷ cells were harvested for determination. The cells were washed with cold PBS twice, and then lysis solution was added to release intracellular H₂O₂. Finally, the mixtures were centrifuged at 14,000 *g* at 4 °C, and the supernatants were collected for determination according to the H₂O₂ assay kit.

2.7. Hydroxyl radical determination

The hydroxyl radical (\cdot OH) was determined by methylene blue (MB), a hydroxyl radical capturing reagent (the MB could capture the produced \cdot OH and then fade at the wavelength of 640 nm). Hence the amount of \cdot OH was correlated to the absorbance reduction of MB. Briefly, 0.5 mL of different samples were added into 1 mL of 2 mg/mL MB solution, and then 0.5 mL of 200 μ M H₂O₂ was added to initiate the determination reaction. The absorbance of each measurement was determined by a UV-vis spectrophotometry.

2.8. Cellular ROS assays

The ROS assays were performed by ROS assay kits provided by Beyotime. Briefly, the cells were seeded in a 6-wells plate with a density of 10⁶ cells per well. The cells were treated with different drugs for 2 h and then loaded with DCFH-DA for 30 min. The cells were washed with cold PBS, and FCM or CLSM experiments were applied immediately. FITC channel was chosen for FCM and DCF channel was chosen for CLSM.

2.9. Cytotoxicity assay

The cytotoxicity assays were performed *via* the CCK-8 method according to the manufacturer's protocol. Briefly, the cells were counted and seeded into a 96-wells plate with a density of 5000 cells/well. After that, the plate was incubated for 12 h, and the medium was replaced with the drug-containing medium of indicated concentration respectively (6 parallel wells) and incubated for 24 h. Finally, 10 μ L of CCK-8 solution was added to each well and incubated for 2 h. The optical absorption at 450 nm of the plate was determined by a microplate reader (SpectraMax i3x).

2.10. Photothermal properties characterization

The photothermal properties characterizations were referred to in our previous research (Zeng et al., 2018). Briefly, 1 mL of the sample with indicated concentrations was added into 1 cm \times 1 cm quartz cells, and the 808 nm NIR laser (dot size = 1 cm², power = 1 W) was irradiated on the samples vertically. A thermal camera (Fluke) was employed to record the temperature change against time.

2.11. In vitro photothermal therapy study

Cytotoxicity assays and CLSM were employed to evaluate the photothermal anti-tumor effect of BPF_e on MCF-7. For cytotoxicity assays, the cells were seeded in a 96-wells plate with a density of 5000 cells per well. The BPF_e with indicated concentration was added to wells and incubated for 4 h. Then the plate was irradiated by 808 nm NIR laser (1 W, 5 min per well) and incubated for another 20 h and finally evaluated by CCK-8 assays. For CLSM observation, 2 \times 10⁵ cells were seeded in a glass-bottom dish and cultured for 24 h. The BPF_e was then administrated and incubated for 4 h. To observe the laser on-off effect, we employed a pierced foil to control the irradiated area, and the cells were irradiated by NIR laser at 1 W cm⁻¹ for 5 min at the selected area. The cells were incubated for another 6 h and treated with Calcein-AM to detect alive cells under the observation of CLSM.

2.12. In vitro photothermal and chemodynamic therapeutic effect of BPF_eP

To evaluate whether therapeutic activities of PEGylated BPF_e (BPF_eP) were similar to BPF_e, we had performed a cytotoxicity assay and cellular ROS assay to investigate the photothermal and chemodynamic therapeutic effect of BPF_eP. The protocols and conditions were according to previous assays.

2.13. Hemolysis test

A hemolysis test was performed to investigate the safety and biocompatibility of the nano-system. In brief, fresh blood was obtained from SD rats, and then it was centrifuged at 2000 rpm for 10 min to obtain red blood cells. The red blood cells were gently washed by PBS 3–5 times and then diluted by PBS (1:10). 200 μ L diluted red blood cells were then gently added into 800 μ L of test solution. The mixture was incubated for 1 h at 37 °C and centrifuged at 1000 rpm to isolate unbroken RBCs, and the optical density of supernatants was analyzed at 570 nm.

2.14. Xenograft tumor models

The assays of animal experiments were under the guidance of the Administrative Committee on Animal Research in Sun Yat-sen University. To establish xenograft models, 0.1 mL of MCF-7 cell suspensions in PBS (2 \times 10⁶ cells for each mouse) were subcutaneously injected to the outer side to establish tumors.

2.15. In vivo photothermal therapy

The MCF-7 tumor-bearing mice with a tumor volume of around 300 mm³ were intravenously injected with 200 μ L of PBS, BPF_e and BPF_eP, respectively. After 12 h administration, the mice were anesthetized and irradiated by 808 nm NIR laser with a power of 1.5 W cm⁻¹ for 5 min. The tumor temperature was monitored instantly *via* the photothermal

imaging camera to determine the therapeutic effect and avoid overtreatment.

2.16. In vivo anti-tumor effect and biosafety examination

The MCF-7 tumor-bearing mice were randomly grouped when the average tumor size reached 100 mm^3 . The Control group was intravenously injected with $200\ \mu\text{L}$ of PBS; NIR group was intravenously injected with $200\ \mu\text{L}$ of PBS and treated with 808 nm NIR laser for 5 min after administration; BPFEP group was intravenously injected with $200\ \mu\text{L}$ of BPFEP; BPFEP + NIR group was intravenously injected with $200\ \mu\text{L}$ of BPFEP and treated with 808 nm NIR laser for 5 min after administration. All the groups were administrated with indicated drugs on days 1, 3 and 7, and the BPFEP group was treated with NIR on days 4 and 8 (12 h after each administration).

The tumor volumes and body weights were recorded every two days to examine the anti-tumor effect of each group. The tumor volumes (V) were calculated as $V = \text{Length} \times \text{Width} \times \text{Width}/2$. The tumor tissues and major organs of the participated mice were harvested for further observation. A picture of the excised tumors was taken. The major organs were then fixed in 4% paraformaldehyde for further H&E staining.

2.17. Statistical methods

The experimental data were presented as mean \pm standard deviation. Statistical analysis was performed *via* one-way ANOVA on Origin Pro 2021 (OriginLab Corporation). Different statistical significance was presented as $p < .05$ (*), $p < .01$ (**) and $p < .001$ (***).

3. Results and discussion

3.1. Characterizations of BPFfe

To prove the successful preparation of BPFfe, we firstly observed the BPNS and BPFfe *via* transmission electron microscope (TEM) (Figure 2a,b). TEM images have shown that both materials were two-dimensional sheet structures. EDS mapping images (Figure 2c) had proved that the Fe and O elements were distributed on the nanosheets, which indicated the success of BPNS phosphorylation and Fe ion decoration. We next measured the thickness of BPNS and BPFfe by atom force microscopy (AFM) (Figure 2d,f). According to the height information (Figure 2e,g), the average thickness of BPFfe was 25.3 nm , which was higher than that of BPNS (12.5 nm). AFM experiments illustrated that deposition of Fe ions could increase the thickness of nanosheets. Then we determined the zeta potential and hydrodynamic particle size of the BPNS and BPFfe. Zeta potential (Figure 2h) revealed that the negative charge potential of BPNS was reduced since depositing Fe ions. Dynamic light scattering (DLS) (Figure 2i) showed that the effective size of BPNS and BPFfe was $151.7 \pm 3.3\text{ nm}$ and $189.1 \pm 3.0\text{ nm}$, and the PDI were 0.238

and 0.227 , respectively. The increase in the particle size also indicated the successful preparation of BPFfe.

We further performed XPS to study the surface composition of BPFfe. P 2p scan of BPFfe (Figure 2j) revealed the presence of P-O bond, a phosphorylated form of P. Fe 2p scan of BPFfe (Figure 2k) showed the presence of Fe^{2+} and Fe^{3+} , and the atomic ratio between Fe^{2+} and Fe^{3+} was calculated as 1.67 . Therefore, the Fe ions have mainly existed as iron (II) phosphates on the surface of BPNS. Thorough atomic ratio analysis of XPS was given in Table S1. Besides, the Fe to P mass ratio of BPFfe was 1.041 determined by ICP-MS, which indicated that such *in situ* mineralization method could effectively load Fe ions. The prepared sample and optical absorption spectra were shown in Figure S1, and the linear relationship of BPFfe between concentration and absorption was shown in Figure S2. All these results indicated that we successfully prepared BPFfe by *in situ* mineralization. Moreover, we found that the BPFfe had faster degradation under acidic pH of 6.0 than pH of 7.0 which indicated that the BPFfe could respond to tumor acidic environment and degrade to release Fe ions (Figure S3).

3.2. Cell uptake of BPFfe

In order to examine cellular uptake of BPFfe, we labeled doxorubicin (DOX) on BPFfe for its easy stack on BP and stable fluorescence even after loading. 4T1 and MCF-7 cell lines were chosen to examine the uptake efficiency. CLSM images (Figure S4a) indicated that the ingested BPFfe was distributed in the cytosol. FCM analysis (Figure S4b) showed the proportional relationship between time and uptake amount. As a result, the BPFfe could be internalized by the tumor cells efficiently.

3.3. Hydroxyl radical production mediated by BPFfe

The theoretical basis that BPFfe could selectively inhibit tumor cells was the H_2O_2 concentration difference between tumor and normal cells. Hence, we first validated the intracellular H_2O_2 concentration difference between tumor (MCF-7, Hep1-6 and B16F10) and normal (NCM460) cell lines (Figure 3a). The results indicated that such a concentration difference did exist. To evaluate the $\cdot\text{OH}$ production of BPFfe *in vitro*, MB was employed to detect the $\cdot\text{OH}$. The decreased absorbance of MB (Figure 3b) manifested that the BPFfe could catalyze H_2O_2 to produce $\cdot\text{OH}$ in a concentration-dependent manner. Moreover, our BPFfe showed better $\cdot\text{OH}$ production than previously published Fe_3O_4 nanoparticles (as shown in Figure S5), which might derive from the faster release of Fe ions of BPFfe than Fe_3O_4 . We also compared the $\cdot\text{OH}$ production ability of bare BPNS with BPFfe. The results (Figure S6a,b) demonstrated that BPFfe generated much more $\cdot\text{OH}$ than BPNS, which indicated that the Fe deposition contributed to the production of $\cdot\text{OH}$.

Then, we investigated the ROS levels in the cellular level *via* DCFH-DA, a ROS probe, after treatment with different drugs. Both FCM and CLSM analyses revealed that the BPFfe increased the intracellular ROS in tumor cells while having a

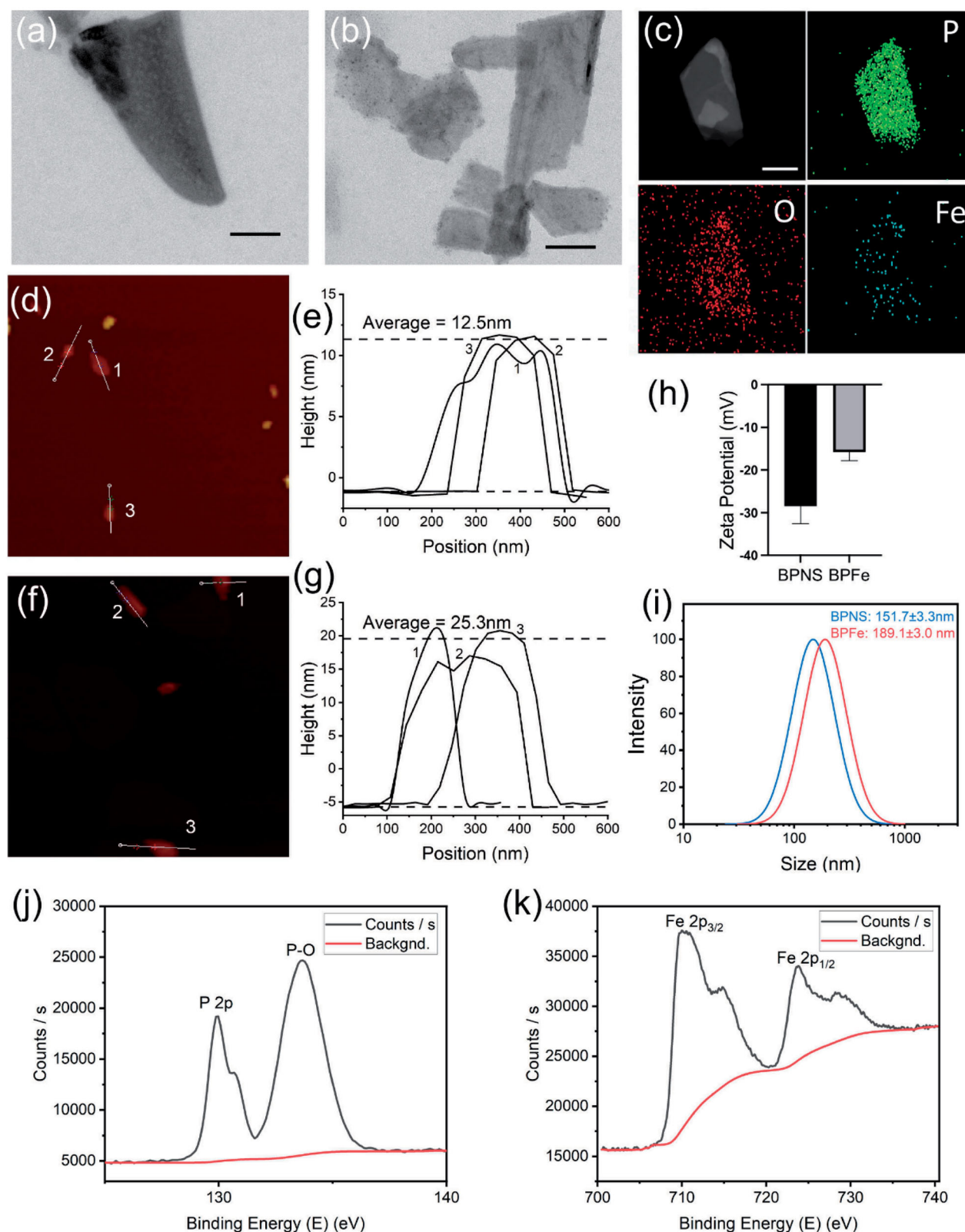


Figure 2. Characterization of BPFe. (a) TEM image of BPNS (scale bar = 100 nm); (b) TEM image of BPFe (scale bar = 100 nm); (c) EDS mapping images of BPFe (scale bar = 100 nm); AFM image (d) and height analysis (e) of BPNS; AFM image (f) and height analysis (g) of BPFe; (h) Zeta potential of BPNS and BPFe; (i) Particle size distributions of BPNS and BPFe; (j) P 2p scan of XPS survey on BPFe; (k) Fe 2p scan of XPS survey on BPFe.

weak influence on normal cells. A representative example, MCF-7, was shown in Figure 3(c,d). Similar results were found in other tumor cells, like Hep1-6, B16F10 (Figure S7). Meanwhile, the ROS level remained low in normal cells after

treatment of BPFe, like NCM460 (Figure 3d). These results indicated that BPFe was able to utilize the different levels of H_2O_2 between cancer and normal cells to selectively generate $\cdot OH$ and increase the ROS stress in tumor cells.

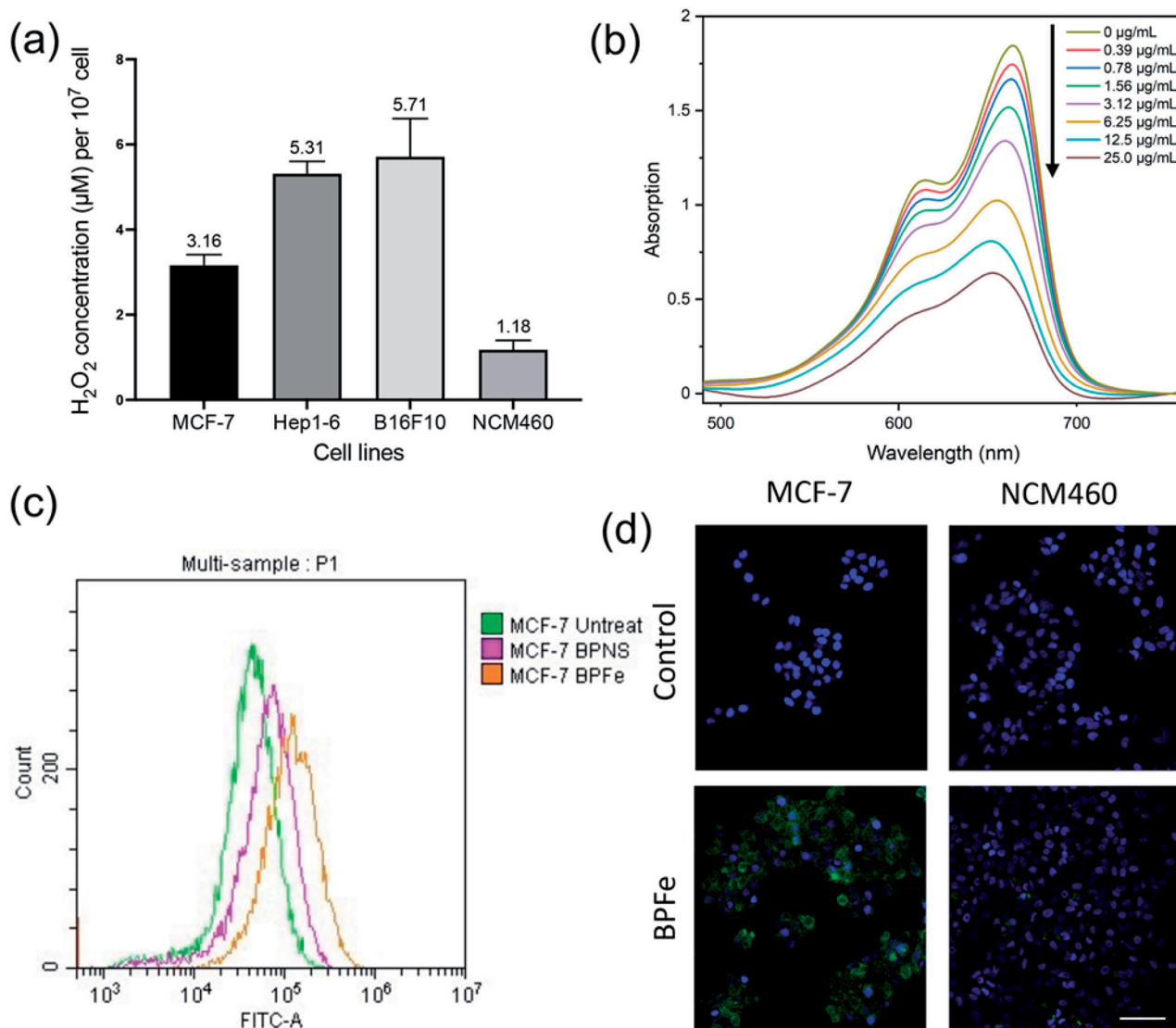


Figure 3. *In vitro* ROS and •OH assays. The BPF could generate more •OH in tumor cells with higher H₂O₂ levels compared to normal mammalian cells. (a) H₂O₂ concentration (per 10⁷ cells) of selected cell lines. (b) The absorbance of MB after treatment with the indicated concentration of BPF. (c) FCM analysis of MCF-7 ROS level after treated with BPNS or BPF. (d) Confocal images of DCFH fluorescence intensity of MCF-7 and NCM460 (Blue channel: DAPI, green channel: DCFH, scale bar = 100 µm).

3.4. Cytotoxicity of BPF

Bare BPNS was known for its good biocompatibility and safety, which did not show obvious toxicity in both tumor and normal cells (Figure S8). Unlike BPNS, BPF showed relatively higher toxicity in tumor cells (IC₅₀ from 2.996 µg/mL to 6.833 µg/mL, Figure 4(a–c)) than normal cells (IC₅₀ more than 50 µg/mL, Figure 4c). According to the determined H₂O₂ level (Figure 3a), we compared the relationship between H₂O₂ level and IC₅₀. As shown in Figure S9, BPF exhibited higher cytotoxicity in H₂O₂ overproduced tumor cells than normal cells, because it could induce Fenton reaction to generate more hazardous •OH in these tumor cells.

Considering the ROS-level shown in Figure 3(a), we concluded that tumor cells were more sensitive to BPF, because the Fenton reaction could cause strong oxidative stress in tumor cells. On the contrary, the normal cells could avoid such oxidative stress for their low H₂O₂ level.

3.5. *In vitro* photothermal therapy effect of BPF

Other than its selectivity between tumor and normal cell lines, the BPF also showed good photothermal activity. We examined the photothermal properties of BPF under 808 nm NIR laser irradiation (1 W cm⁻¹). After irradiation for 10 min, BPF could increase 24.3 °C with the concentration of 250 µg/mL (Figure 5a), which was higher than that of BPNS (23.3 °C, as shown in Figure S10). Besides, we investigated the photothermal stability of BPF: 125 µg/mL BPF was irradiated under 808 nm NIR laser irradiation (1 W cm⁻¹) for 10 min and placed for cooling. As shown in Figure 5(b), the BPF could still rise back to the initial maximum temperature even after 5 cycles of irradiation.

We next examined the photothermal cytotoxicity on the MCF-7 cell line. To observe the photothermal on-off effect of BPF, we partially irradiated the BPF treated cells, and stained the live cells with Calcein-AM. Figure 5(c) obviously

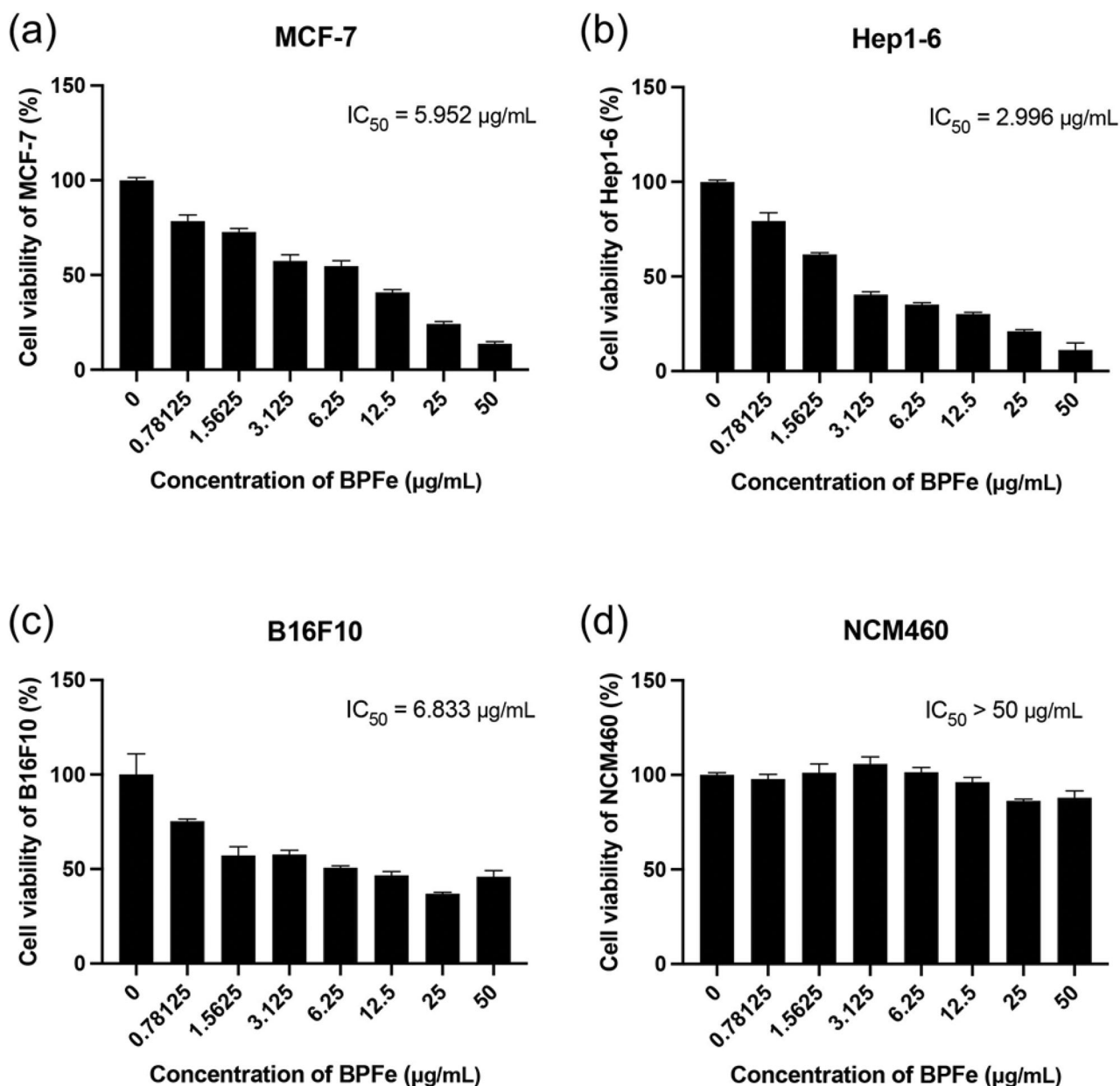


Figure 4. Cytotoxicity assays of BPFc. Tumor cell lines: (a) MCF-7, (b) Hep 1–6, (c) B16F10. Normal cell line: (d) NCM460.

showed that rare cells were alive in the irradiated area. Besides, cytotoxicity assays had demonstrated that the photothermal treatment decreased the IC_{50} of BPFc by 5-fold (from 5.952 to 1.109 $\mu\text{g/mL}$) (Figure 5d). Moreover, we performed apoptosis analysis on MCF-7 to explore the cell death mechanism induced by BPFc. The results (Figure S11) demonstrated that BPFc could induce tumor cell apoptosis, and sole NIR irradiation treatment was nontoxic. As a result, BPFc showed an enhanced tumor-killing effect while combined with NIR irradiation.

3.6. In vitro photothermal and chemodynamic effect of BPFcP

PEGylation is a widely used surface modification in nano-system, which is proved to enhance biocompatibility and blood

circulation behaviors. We employed PEG-NH₂ to decorate on BPFc to prepare BPFcP, and hydrodynamic particle size and zeta potential of BPFcP were characterized. The results (Figure S12) showed that the particle size of BPFcP increased to 295.2 nm and the negative charge of BPFc decreased in BPFcP, which indicated the successful decoration of PEG. Besides, the BPFcP also showed similar photothermal properties with BPFc (Figure S13).

We performed cytotoxicity assays to determine the anti-tumor activities of BPFcP. The results (Figure 6a,b) demonstrated that the BPFcP had similar chemodynamic and photothermal effects to BPFc. Furthermore, we performed CLSM to determine ROS generation. Figure 6(c) demonstrated that the BPFcP could generate adequate intracellular ROS in dark, meanwhile, more ROS was detected after being treated with 808 nm NIR. As a result, the NIR treated BPFcP group showed

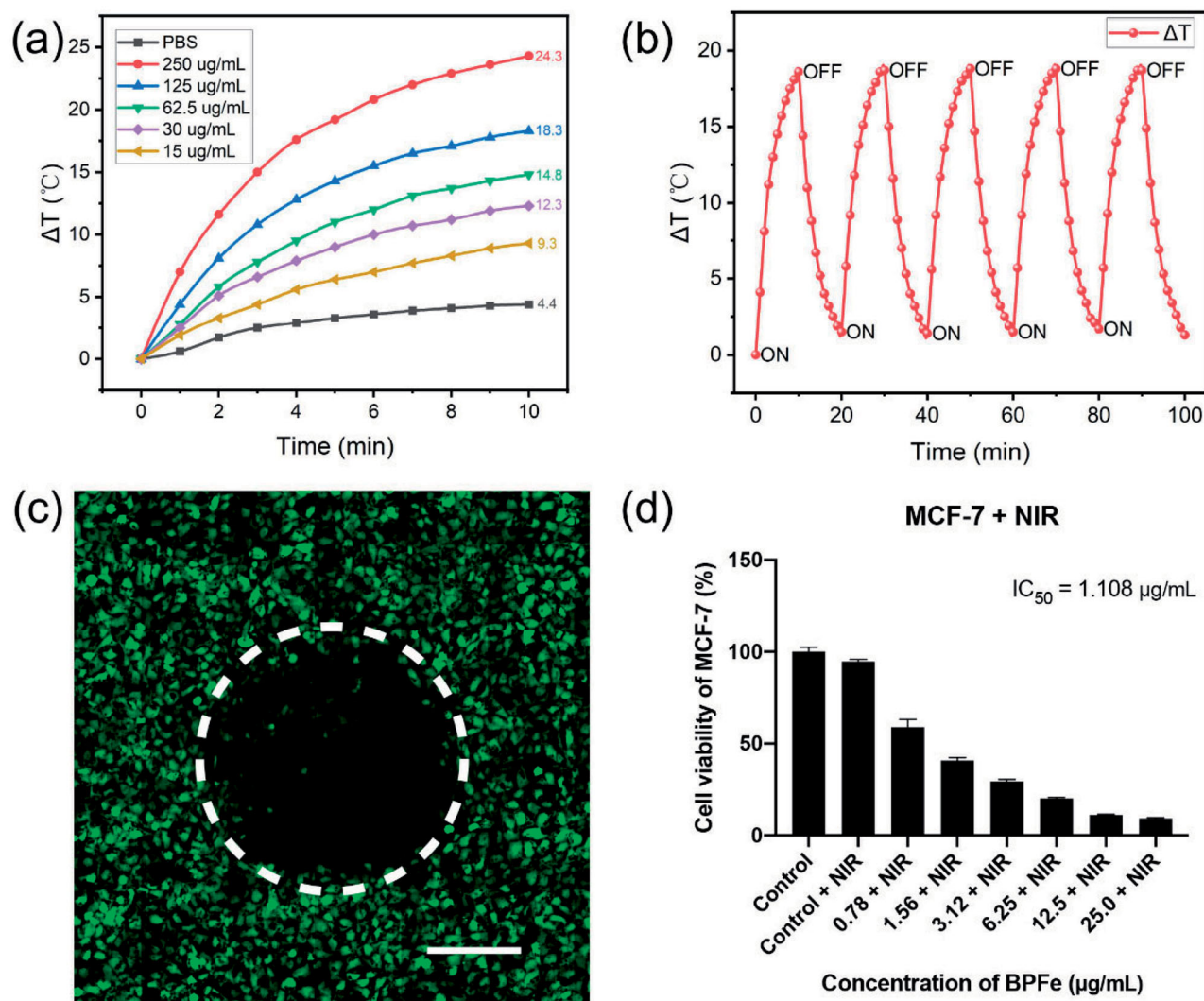


Figure 5. The photothermal properties of BPFc. (a) Temperature elevation curves of BPFc with different concentrations under 808 nm laser (1 W cm^{-2}). (b) Photothermal stability of BPFc for five lasers on/off cycles under 808 nm laser (1 W cm^{-2}). (c) CLSM images of MCF-7 after being treated with BPFc and NIR irradiation, the green fluorescence was Calcein-AM stained live cells (Scale bar = 200 μm). (d) Cell viability of MCF-7 after treatment with BPFc and NIR irradiation.

the highest ROS level, which indicated that the BPFcP group could realize successful chemodynamic and photothermal combinations *in vitro*.

3.7. Hemolysis assays of BPFcP

We performed hemolysis assays to investigate the safety of our nano-system before *in vivo* study. The BPFc and BPFcP with concentrations of 1.56–100 $\mu\text{g/mL}$ were mixed with red blood cells. After incubating for 1 hour at 37 $^{\circ}\text{C}$, the samples were centrifuged to observe the hemolysis. As shown in Figure 7, both BPFc and BPFcP did not show obvious hemolysis compared with positive control. The hemolysis rates were calculated through the optical density of supernatants at 570 nm. All the hemolysis rates were below 5%, which indicated the safety of BPFcP.

3.8. In vivo photothermal imaging

Previous results confirmed that BPFcP had good biocompatibility and excellent photothermal properties *in vitro*. We

further performed *in vivo* photothermal imaging assays to observe the photothermal effects of BPFcP. As shown in Figure 8, the PBS group increased up to 41.1 $^{\circ}\text{C}$. The temperature of the BPFcP group increased to 60.1 $^{\circ}\text{C}$, which was higher than that of BPFc (48.5 $^{\circ}\text{C}$). This indicated that the PEGylation could endow the BPFc with the long-circulation ability and higher stability *in vivo*. Such a feature of BPFcP could increase the accumulation of BPFcP in the tumor site.

3.9. In vivo anti-tumor effect of BPFcP

We further tested the chemodynamic and photothermal synergistic treatment effects on tumor-bearing mice. The treatment procedures were shown in Figure 9(a): the MCF-7 xenograft tumor-bearing mice were administrated with saline or BPFcP at days 1, 3 and 7, and the 808 nm NIR irradiation was given at days 4 and 8 for NIR-involved groups. After 2 weeks of treatment, we excised the tumors from each group, which were compared in Figure 9(b), and found that there were two mice without a residual tumor in BPFcP + NIR group. The tumor weight is shown in

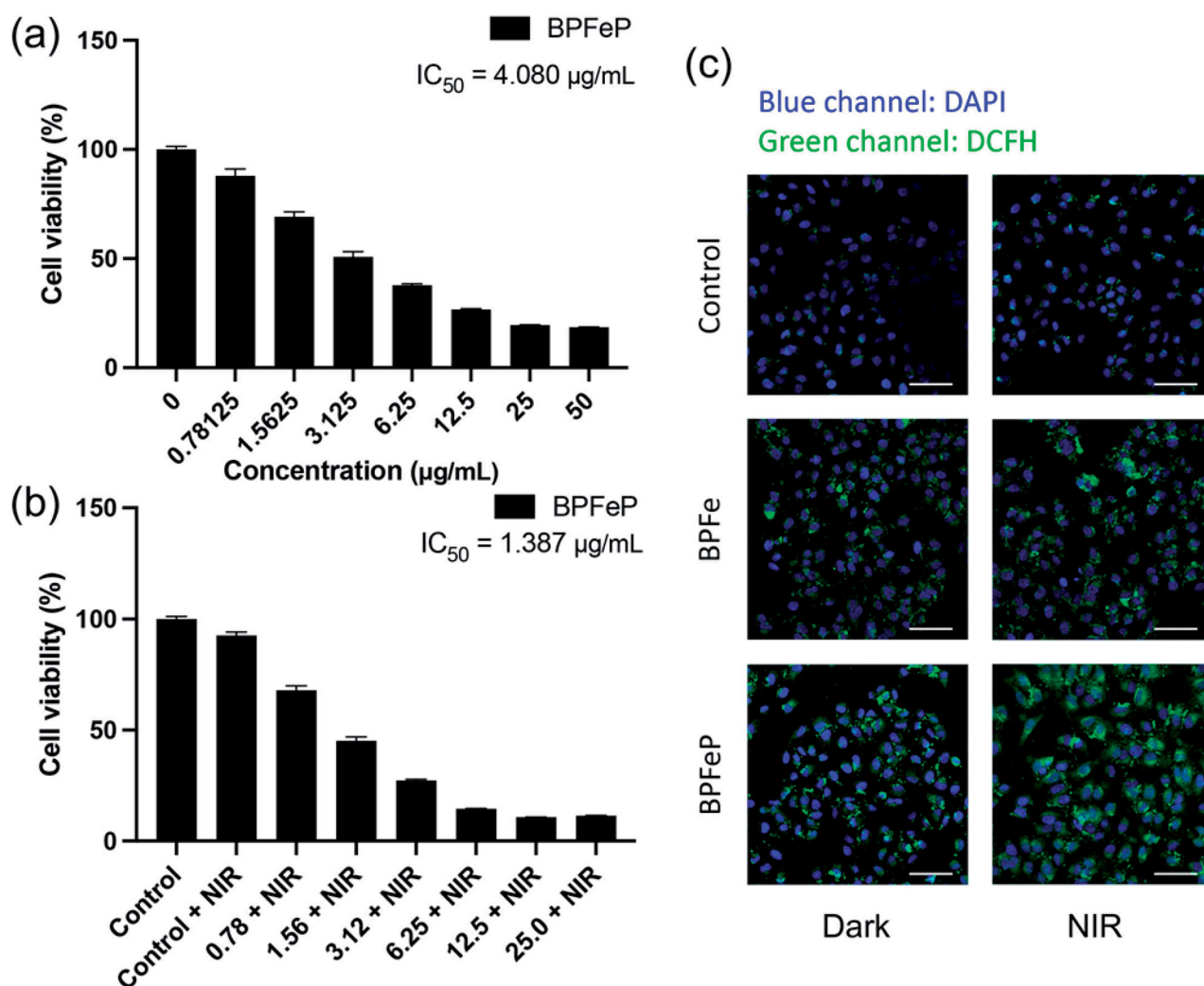


Figure 6. BPFep showed similar therapeutic activities to BPFep. (a) Cell viability of MCF-7 after treatment with the indicated concentration of BPFep. (b) Cell viability of MCF-7 after treatment with the indicated concentration of BPFep and NIR irradiation (under 808 nm laser, 1 W cm^{-1} , 5 min). (c) CLSM images of MCF-7 for observing intracellular ROS generation under different treatments (Dark group was not treated with NIR, NIR group was treated with 808 nm laser, 1 W cm^{-1} , 5 min. Scale bar = $100 \mu\text{m}$).

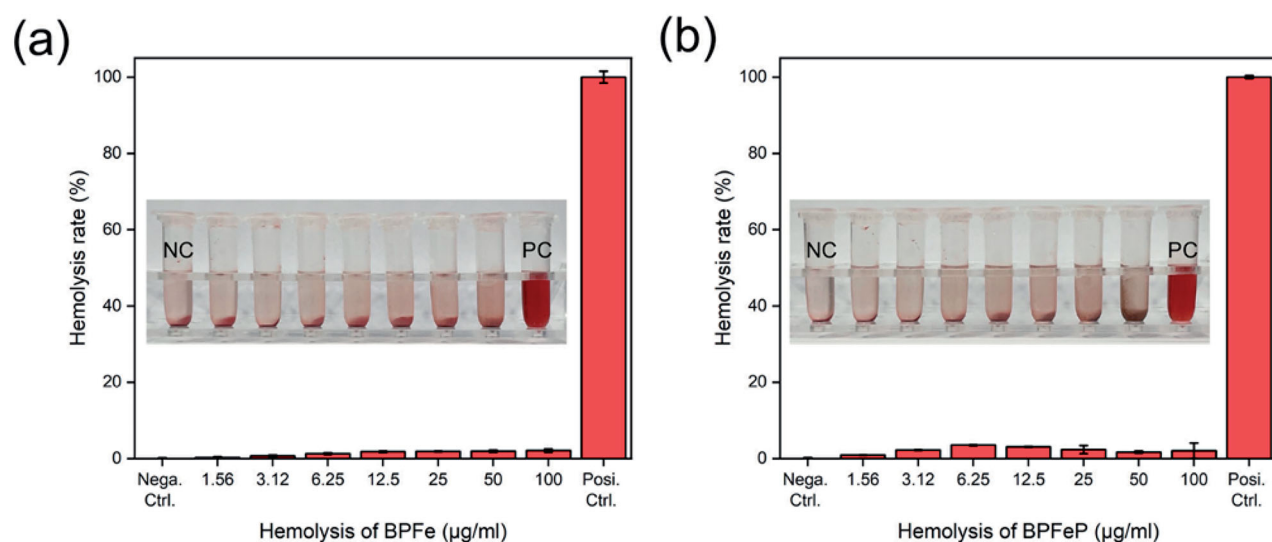


Figure 7. Hemolysis assays to (a) BPFep and (b) BPFep. Tubes in the picture were listed as NC (negative control), drugs of indicated concentration and PC (positive control).

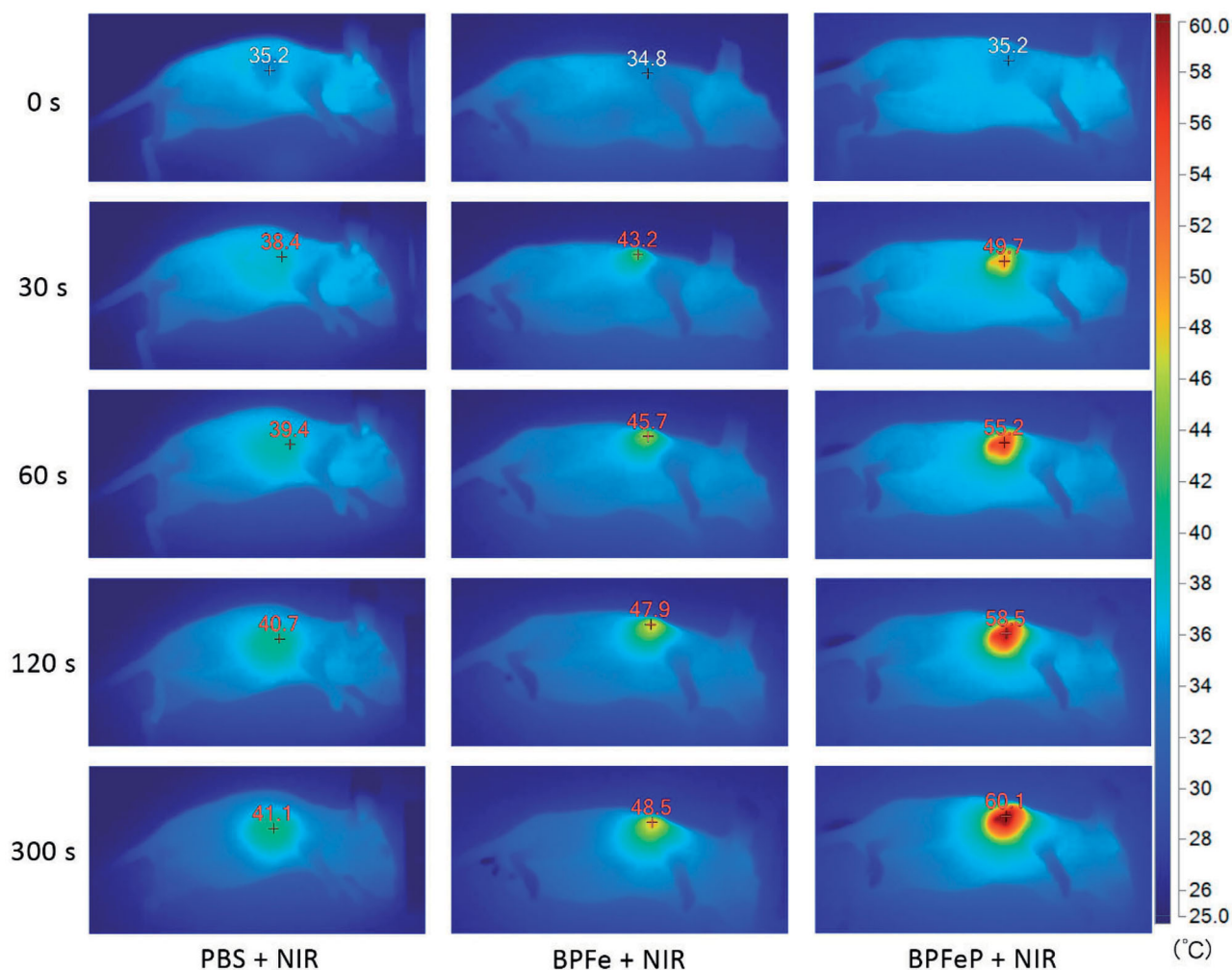


Figure 8. Photothermal images of MCF-7 tumor-bearing mice irradiated via 808 nm NIR laser after 12 h of drug administration.

Figure 9(d) manifested similar results. The tumor growth curve (Figure 9c) also demonstrated the anti-tumor effect of BPFcP. Although the tumors were not completely controlled after sole treatment of BPFcP, a combination of chemodynamic and photothermal therapy inhibited the tumor growth excellently. The body weight (Figure 9e) of the mice did not show obviously losing during the whole treatment. Moreover, the H&E staining results (Figure S14) showed no obvious lesion on major organs of all groups, which proved its good biocompatibility and safety.

4. Conclusions

Many differences in the tumor microenvironment allowed scientists to distinguish tumor tissues or cells from normal ones. Overproduction of H_2O_2 , acidic extracellular environment and hypoxia condition are well-established biomarkers of tumors. The chemodynamic therapy that utilizes these features has become important antitumor therapeutics. However, the slow release of active Fe ions from traditional Fe-based CDT-inducers, like iron oxide nanoparticles and iron

mineral nanoparticles, limited the outcome of CDT. Recently, an amorphous Fe-based nano-system showed fast release of Fe ions and excellent chemodynamic effect, which indicated the importance of developing a novel Fe-based CDT inducer. Herein, we rationally designed iron-mineralized black phosphorene nano-systems to gain BPFcP. BPFcP directly loaded individual Fe ions on BPNS and showed a much better Fenton effect than traditional Fe_3O_4 nanoparticles, which might owe to the easy release of Fe ions from BPFcP. BPFcP exhibited good biosafety and biocompatibility to normal mammalian cells. Meanwhile, BPFcP selectively killed tumor cells with higher H_2O_2 levels *in vitro*. Further experiments with tumor-bearing mice indicated that BPFcP selectively richened in tumor sites and showed an excellent antitumor effect *in vivo*. The combination of PTT and BPFcP further improved the antitumor outcome. As a result, this study provided a platform to treat tumors by combining chemodynamic therapy and photothermal therapy to ablate solid tumors. The excellent photothermal property of BPFcP endowed such nano-system with on-demand antitumor ability, which ensured the spatiotemporal accuracy of cancer therapy.

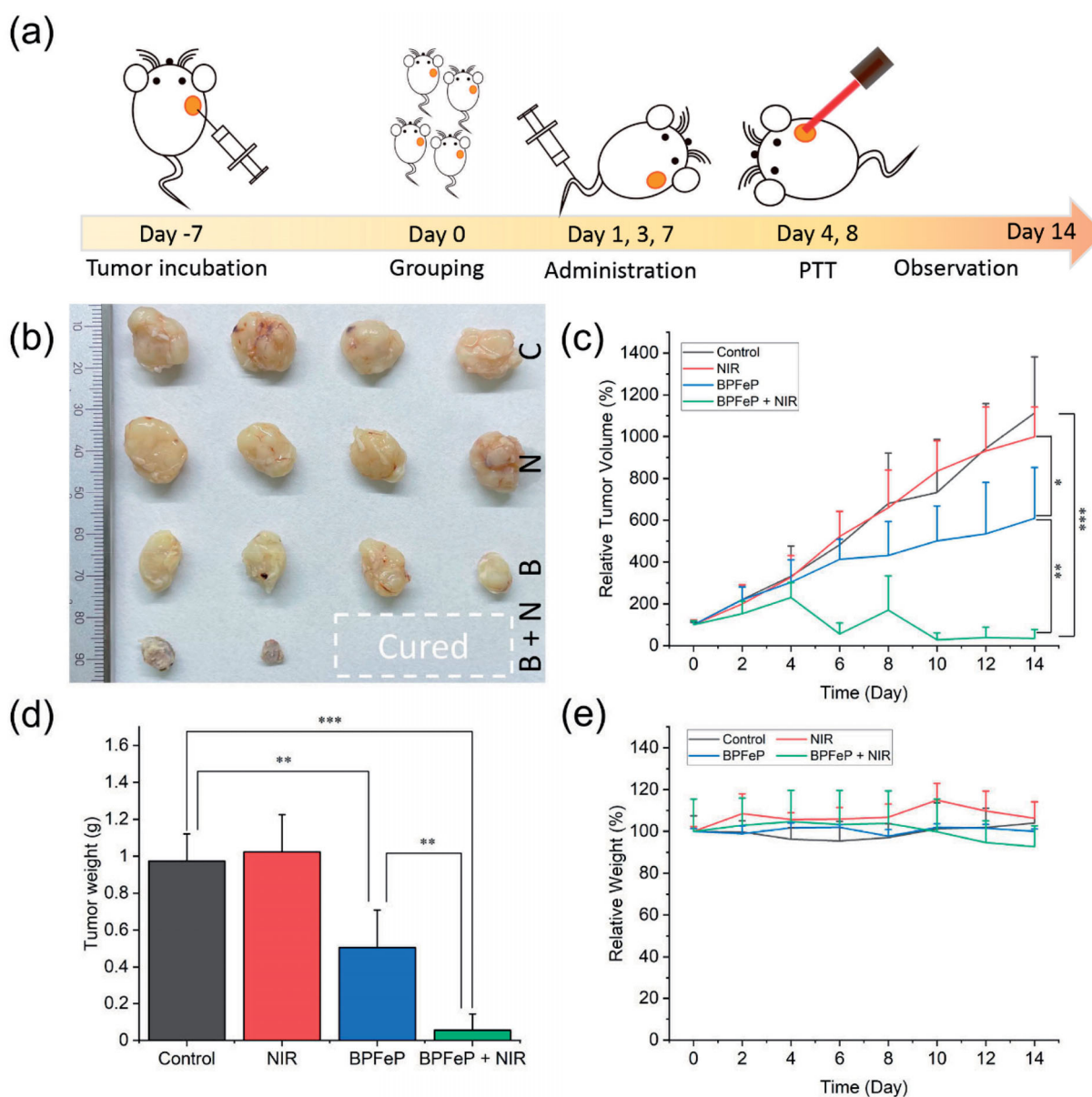


Figure 9. *In vivo* chemodynamic and photothermal synergistic treatment. (a) Schematic illustration of treatment procedures. (b) Excised tumors after 2 weeks of treatment. The C, N, B and B + N represented as Control, NIR, BPF_eP and BPF_eP + NIR, respectively. (c) Tumor volume of mice after indicated treatment. (d) Weight of excised tumor. (e) Mice body weight change. ($n = 4$, different p was marked as *, **, *** while $p < .05$, .01 and .001.)

Author contributions

Mei L. and Li Q. designed this study. Shi Z. carried out the project and data analysis. Zhang F., Shi Z. and Li Q. performed *in vitro* experiments. Shi Z., Tang J., Lin C., and Chen T. performed *in vivo* experiments. Shi Z. and Li Q. wrote the manuscript, and Luan P., Huang Y., Xin Z. and Mei L. provided revisions.

Disclosure statement

The authors declare that they have no known competing financial interests or personal relationships that could have appeared to influence the work reported in this paper.

Funding

This work was supported by the National Natural Science Foundation of China (22007106 and 31922042), the Key Project of Basic Research of Shenzhen (JCYJ20200109113603854), the International Cooperation

Research Project of Shenzhen (Ping Luan), the Fundamental Research Funds for the Central Universities (2021-RC310-005, 2020-RC320-002 and 2019PT320028) and Chinese Academy of Medical Sciences Innovation Fund for Medical Sciences (2021-I2M-1-058).

References

- An D, Fu J, Zhang B, et al. (2021). NIR-II responsive inorganic 2D nano-materials for cancer photothermal therapy: recent advances and future challenges. *Adv Funct Mater* 31:2101625.
- Chen Q, Zhou J, Chen Z, et al. (2019). Tumor-specific expansion of oxidative stress by glutathione depletion and use of a Fenton nanoagent for enhanced chemodynamic therapy. *ACS Appl Mater Interfaces* 11: 30551–65.
- Chen X, Zhang H, Zhang M, et al. (2020). Amorphous Fe-Based nano-agents for self-enhanced chemodynamic therapy by re-establishing tumor acidosis. *Adv Funct Mater* 30:1908365.

- Ding B, Zheng P, Ma P, Lin J. (2020). Manganese oxide nanomaterials: synthesis, properties, and theranostic applications. *Adv Mater* 32: e1905823.
- Dong Z, Feng L, Chao Y, et al. (2019). Amplification of tumor oxidative stresses with liposomal Fenton catalyst and glutathione inhibitor for enhanced cancer chemotherapy and radiotherapy. *Nano Lett* 19: 805–15.
- Fan JX, Peng MY, Wang H, et al. (2019). Engineered bacterial bioreactor for tumor therapy via Fenton-like reaction with localized H₂ O₂ generation. *Adv Mater* 31:e1808278.
- Feng W, Han X, Wang R, et al. (2019). Nanocatalysts-augmented and photothermal-enhanced tumor-specific sequential nanocatalytic therapy in both NIR-I and NIR-II biowindows. *Adv Mater* 31:e1805919.
- Hanahan D, Weinberg RA. (2011). Hallmarks of cancer: the next generation. *Cell* 144:646–74.
- Hu K, Xie L, Zhang Y, et al. (2020). Marriage of black phosphorus and Cu(2+) as effective photothermal agents for PET-guided combination cancer therapy. *Nat Commun* 11:2778.
- Hu P, Wu T, Fan W, et al. (2017). Near infrared-assisted Fenton reaction for tumor-specific and mitochondrial DNA-targeted photochemotherapy. *Biomaterials* 141:86–95.
- Huo M, Wang L, Chen Y, Shi J. (2017). Tumor-selective catalytic nanomedicine by nanocatalyst delivery. *Nat Commun* 8:357.
- Kuntz KL, Wells RA, Hu J, et al. (2017). Control of surface and edge oxidation on phosphorene. *ACS Appl Mater Interfaces* 9:9126–35.
- Lei S, Chen J, Zeng K, et al. (2019). Visual dual chemodynamic/photothermal therapeutic nanoplateform based on superoxide dismutase plus Prussian blue. *Nano Res* 12:1071–82.
- Li C, Wang JC, Wang YG, et al. (2019). Recent progress in drug delivery. *Acta Pharm Sin B* 9:1145–62.
- Li S, Shang L, Xu B, et al. (2019). A nanozyme with photo-enhanced dual enzyme-like activities for deep pancreatic cancer therapy. *Angew Chem Int Ed Engl* 58:12624–31.
- Li T, Zhou J, Wang L, et al. (2019). Photo-Fenton-like metal-protein self-assemblies as multifunctional tumor theranostic agent. *Adv Health Mater* 8:e1900192.
- Li WP, Su CH, Chang YC, et al. (2016). Ultrasound-induced reactive oxygen species mediated therapy and imaging using a Fenton reaction activable polymersome. *ACS Nano* 10:2017–27.
- Liang X, Ye XY, Wang C, et al. (2019). Photothermal cancer immunotherapy by erythrocyte membrane-coated black phosphorus formulation. *J Control Release* 296:150–61.
- Lin LS, Song J, Song L, et al. (2018). Simultaneous Fenton-like ion delivery and glutathione depletion by MnO₂-based nanoagent to enhance chemodynamic therapy. *Angew Chem Int Ed Engl* 57: 4902–6.
- Liu G, Tsai HI, Zeng XW, et al. (2019). Black phosphorus nanosheets-based stable drug delivery system via drug-self-stabilization for combined photothermal and chemo cancer therapy. *Chem Eng J* 375:10.
- Liu T, Liu W, Zhang M, et al. (2018). Ferrous-supply-regeneration nanoen-gineering for cancer-cell-specific ferroptosis in combination with imaging-guided photodynamic therapy. *ACS Nano* 12:12181–92.
- Liu Y, Zhen W, Wang Y, et al. (2019). One-dimensional Fe₂P acts as a Fenton agent in response to NIR II light and ultrasound for deep tumor synergetic theranostics. *Angew Chem Int Ed Engl* 58:2407–12.
- Luo M, Fan T, Zhou Y, et al. (2019). 2D black phosphorus-based biomedical applications. *Adv Funct Mater* 29:1808306.
- Luo MM, Cheng W, Zeng XW, et al. (2019). Folic acid-functionalized black phosphorus quantum dots for targeted chemo-photothermal combination cancer therapy. *Pharmaceutics* 11:242.
- Luo MM, Zhou Y, Gao NS, et al. (2020). Mesenchymal stem cells transporting black phosphorus-based biocompatible nanospheres: active trojan horse for enhanced photothermal cancer therapy. *Chem Eng J* 385:11.
- Pan C, Ou M, Cheng Q, et al. (2020a). Z-scheme heterojunction functionalized pyrite nanosheets for modulating tumor microenvironment and strengthening photo/chemodynamic therapeutic effects. *Adv Funct Mater* 30:1906466.
- Pan T, Fu W, Xin H, et al. (2020b). Calcium phosphate mineralized black phosphorous with enhanced functionality and anticancer bioactivity. *Adv Funct Mater* 30:2003069.
- Qiu M, Wang D, Liang W, et al. (2018). Novel concept of the smart NIR-light-controlled drug release of black phosphorus nanostructure for cancer therapy. *Proc Natl Acad Sci USA* 115:501–6.
- Saravanakumar G, Kim J, Kim WJ. (2017). Reactive-oxygen-species-responsive drug delivery systems: promises and challenges. *Adv Sci* 4: 1600124.
- Shi Z, Li Q, Mei L. (2020). pH-Sensitive nanoscale materials as robust drug delivery systems for cancer therapy. *Chin. Chem. Lett* 31: 1345–56.
- Shi Z, Zhou Y, Fan T, et al. (2020). Inorganic nano-carriers based smart drug delivery systems for tumor therapy. *Smart Materials in Medicine* 1:32–47.
- Sun Z, Xie H, Tang S, et al. (2015). Ultrasmall black phosphorus quantum dots: synthesis and use as photothermal agents. *Angew Chem Int Ed Engl* 54:11526–30.
- Tang Z, Zhao P, Wang H, et al. (2021). Biomedicine meets Fenton chemistry. *Chem Rev* 121:1981–2019.
- Tao W, Zhu X, Yu X, et al. (2017). Black phosphorus nanosheets as a robust delivery platform for cancer theranostics. *Adv Mater* 29: 1603276.
- Trachootham D, Alexandre J, Huang P. (2009). Targeting cancer cells by ROS-mediated mechanisms: a radical therapeutic approach? *Nat Rev Drug Discov* 8:579–91.
- Wang H, Yang XZ, Shao W, et al. (2015). Ultrathin black phosphorus nanosheets for efficient singlet oxygen generation. *J Am Chem Soc* 137:11376–82.
- Wang S, Yu G, Wang Z, et al. (2019). Enhanced antitumor efficacy by a cascade of reactive oxygen species generation and drug release. *Angew Chem Int Ed Engl* 58:14758–63.
- Wang X, Zhong X, Liu Z, Cheng L. (2020). Recent progress of chemodynamic therapy-induced combination cancer therapy. *Nano Today* 35: 100946.
- Wang XQ, Wang W, Peng M, Zhang XZ. (2021). Free radicals for cancer theranostics. *Biomaterials* 266:120474.
- Wu W, Yu L, Jiang Q, et al. (2019). Enhanced tumor-specific disulfiram chemotherapy by *in situ* Cu(2+) chelation-initiated nontoxicity-to-toxicity transition. *J Am Chem Soc* 141:11531–9.
- Zeng XW, Luo MM, Liu G, et al. (2018). Polydopamine-modified black phosphorous nanocapsule with enhanced stability and photothermal performance for tumor multimodal treatments. *Adv Sci* 5:1800510.
- Zhang C, Bu W, Ni D, et al. (2016). Synthesis of iron nanometallic glasses and their application in cancer therapy by a localized Fenton reaction. *Angew Chem Int Ed Engl* 55:2101–6.